PNAS PNAS PNAS

Gate-tunable carbon nanotube–MoS_2 heterojunction p-n diode

Deep Jariwala[a], Vinod K. Sangwan[a], Chung-Chiang Wu[a], Pradyumna L. Prabhumirashi[a], Michael L. Geier[a], Tobin J. Marks[a,b,1], Lincoln J. Lauhon[a], and Mark C. Hersam[a,b,c,1]

Departments of [a]Materials Science and Engineering, [b]Chemistry, and [c]Medicine, Northwestern University, Evanston, IL 60208

Contributed by Tobin J. Marks, September 12, 2013 (sent for review August 13, 2013)

The p-n junction diode and field-effect transistor are the two most ubiquitous building blocks of modern electronics and optoelectronics. In recent years, the emergence of reduced dimensionality materials has suggested that these components can be scaled down to atomic thicknesses. Although high-performance field-effect devices have been achieved from monolayered materials and their heterostructures, a p-n heterojunction diode derived from ultrathin materials is notably absent and constrains the fabrication of complex electronic and optoelectronic circuits. Here we demonstrate a gate-tunable p-n heterojunction diode using semiconducting single-walled carbon nanotubes (SWCNTs) and single-layer molybdenum disulfide as p-type and n-type semiconductors, respectively. The vertical stacking of these two direct band gap semiconductors forms a heterojunction with electrical characteristics that can be tuned with an applied gate bias to achieve a wide range of charge transport behavior ranging from insulating to rectifying with forward-to-reverse bias current ratios exceeding 10^4. This heterojunction diode also responds strongly to optical irradiation with an external quantum efficiency of 25% and fast photoresponse <15 μs. Because SWCNTs have a diverse range of electrical properties as a function of chirality and an increasing number of atomically thin 2D nanomaterials are being isolated, the gate-tunable p-n heterojunction concept presented here should be widely generalizable to realize diverse ultrathin, high-performance electronics and optoelectronics.

2D transition metal dichalcogenide | single layer MoS_2 | van der Waals heterostructure | rectifier | photodetector

When two semiconductors with an opposite carrier type contact one another, charge transfer occurs across their interface and creates a potential difference determined by the doping profile. In bulk semiconductor p-n junctions, the doping level is primarily controlled via diffusion or implantation of substitutional impurities, which implies minimal control over the doping profile following device fabrication. In contrast, atomically thin semiconductors can be electrostatically doped by applying a bias to a capacitively coupled gate electrode (1–3). The atomically thin structure of these materials also enables doping modulation of the overlying layers in a vertically stacked heterostructure (4). For example, this strategy allows gapless graphene to be used in field-effect tunneling devices in combination with other layered materials (4, 5). Vertical 2D heterostructures have also been used to create high-performance Metal Oxide Semiconductor Field Effect Transistors (MOSFETs) (6), tunneling field-effect transistors (FETs) (4), barristors (7), inverters (8), and memory devices (9, 10), in addition to facilitating the study of novel physical phenomena in layered materials (11–14). Similarly, in-plane graphene heterostructures and controlled doping have served as the basis for unique 2D devices (15–18). Although the nearly perfect 2D structure and low density of states in graphene provide advantages in some heterostructure devices, its gapless nature prevents the formation of a large potential barrier for charge separation and current rectification despite efforts to create in-plane p-n homojunctions by split gating (19). In particular, the lack of distinct monolayer semiconductors with complementary (p and n) polarities has precluded the realization of a gate-tunable heterojunction p-n diode.

In this report, we demonstrate the fabrication and operation of a gate-tunable p-n heterojunction diode using semiconducting single-walled carbon nanotubes (s-SWCNTs) (p-type) (20) and single layer (SL)-MoS_2 (n-type) (21, 22). Fig. 1*A* shows a false-colored SEM of a representative device. A lower-magnification optical micrograph of the same device in Fig. 1*B* shows the n-type (SL-MoS_2) FET, p-n s-SWCNT/SL-MoS_2 heterojunction, and p-type (s-SWCNT) FET from top to bottom. The device fabrication begins by depositing e-beam lithographically defined gold electrodes on SL-MoS_2 flakes that are exfoliated on 300-nm SiO_2/Si wafers (Fig. 1 *C, I*). The SL-MoS_2 FET is electrically isolated by patterning 30-nm alumina via atomic layer deposition (ALD) followed by transfer and patterning of a sorted s-SWCNT thin film (23, 24) (Fig. 1 *C, II*) to yield the final device (Fig. 1 *C, III*). *SI Text* provides further details on the device fabrication.

The ultrathin nature of the heterojunction allows gate tunability of the diode electrical characteristics. Fig. 2*A* shows the output plots of a representative device under different gate biases. The device transitions from a nearly insulating behavior at $V_G = 70$ V to a poorly rectifying state ($r^2 < 60\%$ for fits to the Shockley diode equation) at $V_G = 40$ V to a highly rectifying diode for $V_G \leq 0$ V ($r^2 > 99\%$). For the heterojunction diodes, V_D refers to the bias on the s-SWCNT electrode such that $V_D > 0$ corresponds to forward bias while the electrode in contact with SL-MoS_2 is grounded. The transfer plot further demonstrates the gate tunability of the current through the p-n heterojunction (Fig. 2*B*). The transfer characteristics of the junction (green)

Significance

The p-n junction diode is the most ubiquitous and fundamental building block of modern electronics, with far-reaching applications including integrated circuits, detectors, photovoltaics, and lasers. With the recent discovery and study of atomically thin materials, opportunities exist for adding new functionality to the p-n junction diode. Here we demonstrate that a p-n heterojunction diode based on atomically thin MoS_2 and sorted semiconducting carbon nanotubes yields unprecedented gate tunability in both its electrical and optical properties, which is not observed in the case of bulk semiconductor devices. In addition to enabling advanced electronic and optoelectronic technologies, this p-n heterojunction diode provides new insight into charge transport and separation at atomically thin heterointerfaces.

Author contributions: D.J., V.K.S., T.J.M., L.J.L., and M.C.H. designed research; D.J., V.K.S., C.-C.W., P.L.P., and M.L.G. performed research; D.J., V.K.S., C.-C.W., L.J.L., and M.C.H. analyzed data; and D.J., V.K.S., C.-C.W., P.L.P., M.L.G., T.J.M., L.J.L., and M.C.H. wrote the paper.

The authors declare no conflict of interest.

[1]To whom correspondence may be addressed. E-mail: t-marks@northwestern.edu or m-hersam@northwestern.edu.

This article contains supporting information online at www.pnas.org/lookup/suppl/doi:10.1073/pnas.1317226110/-/DCSupplemental.

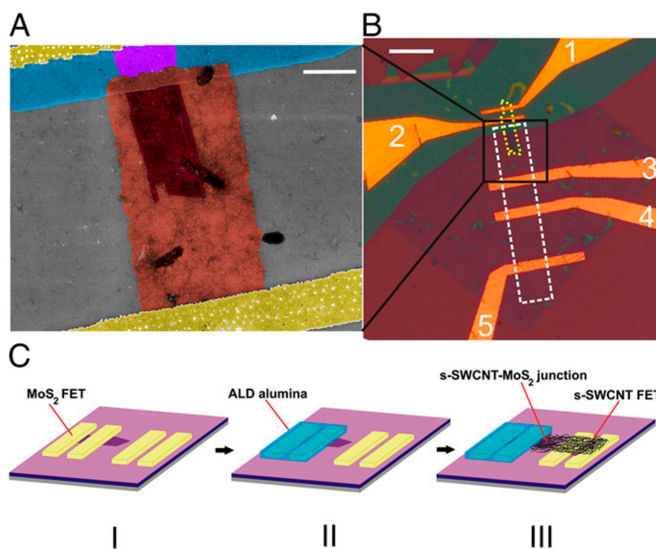

Fig. 1. Microscopy and fabrication of the s-SWCNTs/SL-MoS_2 p-n heterojunction diode. (*A*) False-colored SEM image of the heterojunction diode. (Scale bar, 2.5 μm.) The yellow regions at the top and bottom are the gold electrodes. The patterned alumina (blue region) serves as a mask for insulating a portion of the SL-MoS_2 flake (violet region). The pink region is the patterned random network of s-SWCNTs (p-type) in direct contact with the exposed part of the SL-MoS_2 flake (n-type) to form the p-n heterojunction diode (dark red). (*B*) Optical micrograph showing the device layout at a lower magnification. The dashed yellow boundary indicates the SL-MoS_2 flake, whereas the dashed white rectangle denotes the patterned s-SWCNT film. Electrodes 1 and 2 form the n-type (SL-MoS_2) FET, which is insulated by the patterned alumina film (cyan). Electrodes 2–3 form the p-n heterojunction, whereas 3–4 and 4–5 form p-type s-SWCNT FETs. (Scale bar, 10 μm.) (*C*) Schematic of the fabrication process: (*I*) SL-MoS_2 FET and an extra pair of electrodes are fabricated via e- beam lithography on 300 nm SiO_2/Si. The Si substrate acts as the global back gate. (*II*) The MoS_2 FET is insulated by patterning an alumina film in a liftoff process, followed by (*III*) transfer and patterning of the s-SWCNT network to yield the final device configuration consisting of a top contact SL-MoS_2 FET, bottom contact s-SWCNT FET, and p-n heterojunction.

show an unusual gate voltage dependence, which we refer to as "antiambipolar" behavior. In particular, the maximum conductance occurs near $V_G = 0$, which is the opposite of conventional ambipolar behavior that shows a minimum conductance near $V_G = 0$. The current on/off ratio exceeds 10^4 in the transfer plots, which is suitable for advanced logic applications (*SI Text*). The transfer characteristics of the heterojunction can be qualitatively viewed as a superposition of the p-type s-SWCNT (red) and n-type SL-MoS_2 (blue) FET transfer plots. However, the net current through the heterojunction is smaller than the SL-MoS_2 and s-SWCNT FET transfer characteristics due to the additional resistance at the junction.

This unique transfer characteristic can be viewed as originating from an FET channel consisting of two p and n semiconductors in series. The change in the resistance of each component with gate bias affects the net series resistance leading to the resulting antiambipolar transfer characteristic of the junction. Thus, the junction transfer curve has two off states, representing the depleted state of SL-MoS_2 and s-SWCNTs. Furthermore, the contact resistances of the s-SWCNT film and SL-MoS_2 with Au are relatively small compared with the sheet/channel resistances (25, 26) and thus have negligible effect on the junction characteristics (see *SI Text* for output plots of s-SWCNT and SL-MoS_2 FETs). It is worth noting that the maximum of the junction transfer curve does not exactly coincide with the intersection of the SL-MoS_2 and s-SWCNT transfer curves. This offset can be attributed to hysteresis in the transfer plots and the fact that the SL-MoS_2 FET is encapsulated in alumina, which is known to shift threshold voltage in SL-MoS_2 FETs (21).

An important parameter in characterizing diode characteristics is the ratio of the forward current, $|I_f|$, to the reverse current, $|I_r|$, at the same bias magnitude. Fig. 2*C* shows that $|I_f|/|I_r|$ varies by over five orders of magnitude as a function of gate voltage. Between the two gate bias extremes, the s-SWCNT/SL-MoS_2 heterojunction transitions from an n-n$^+$ junction at $V_G =$ 80 V to a p-n junction at $V_G = -80$ V. The large band gap of SL-MoS_2 (>1.8 eV) (27) compared with that of the s-SWCNTs (~0.7 eV) allows electrostatic depletion of SL-MoS_2 to a lightly n doped (n$^-$) or nearly intrinsic insulating state, thereby leading to $|I_f|/|I_r|$ values exceeding 10^4 at $V_G = -80$ V. On the other hand, the small band gap of the s-SWCNTs allows electrostatic inversion from p-doping to n-doping at large positive V_G, resulting in poor $|I_f|/|I_r|$ values for $V_G > 60$ V. Gate tunable p-n homojunction diodes have been previously fabricated by split gating of individual SWCNTs. However, such homojunctions only allow control over the built-in voltage via differential biases in split gates (28, 29). The present gate tunable p-n heterojunction, on the other hand, is fundamentally different as it has a built-in potential at zero gate bias as evident from the rectifying current (I)-voltage (V) (*I-V*) characteristics (Fig. 2*A*). Furthermore, in this heterojunction, the gate is used to simultaneously tune the doping concentrations of both semiconductors, thereby allowing tunability in the built-in voltage and rectification ratios.

To further understand the gate-dependent modulation of the heterojunction *I-V* curves, we fit them to the Shockley diode equation. The best fit to the Shockley diode equation is observed for $V_G = -40$ V. For other V_G values, either the diode ideality factor (n) is >2 or the fits are poor ($r^2 < 60\%$) (*SI Text*). The disorder at the interface of random network SWCNT films [see atomic force microscopy (AFM) images in *SI Text*] and SL-MoS_2 possibly leads to more recombination, resulting in larger ideality factors compared with the nearly ideal diode behavior in WSe_2/InAs heterojunctions that have a uniform 2D interface (30). The gate dependence of the present diode behavior enables gate-tunable rectifier circuits (Fig. 2*D*), which is a unique feature of the s-SWCNT/SL-MoS_2 heterojunction device that has not been observed in conventional bulk semiconductor diodes (see *SI Text* for further details on measurement techniques).

Both SL-MoS_2 and s-SWCNTs have direct band gaps (31, 32) and exhibit signatures of bound excitonic states in their absorption spectra (2, 31). Therefore, photocurrent generation is expected on optical irradiation of p-n heterojunctions based on these materials. To that end, scanning photocurrent microscopy was used to spatially map the local photoresponse of the s-SWCNT/SL-MoS_2 heterojunction device (Fig. 3*A*). The regions of large negative photocurrent lie in the heterojunction area outlined by the SL-MoS_2 flake (purple) overlapping with the patterned s-SWCNT film (red). No measurable photocurrent is observed from the nonoverlapping regions of either the s-SWCNT film, SL-MoS_2, or the electrical contacts (see *SI Text* for additional details), indicating that the photocurrent measured under uniform illumination is generated by the vertical heterojunction. Photocurrent from Au contacts to s-SWCNT films was not observed in our recent study (33). For the case of two-terminal SL-MoS_2 devices, photocurrent has been observed at the contacts due to band bending (34). However, the band bending at the contacts is opposite to that of the junction, which suppresses the local near-contact photocurrent because charge neutrality cannot be maintained at the injection level used. The spectral dependence of the photocurrent (Fig. 3*B*) corresponds to the absorption peaks of SL-MoS_2 (27) and S_{22} (24) peaks of s-SWCNTs, which demonstrates that this unique heterointerface can induce carrier separation following exciton and/or free carrier generation in either material. The photocurrent generated in the visible portion of the

PNAS PNAS PNAS PNAS

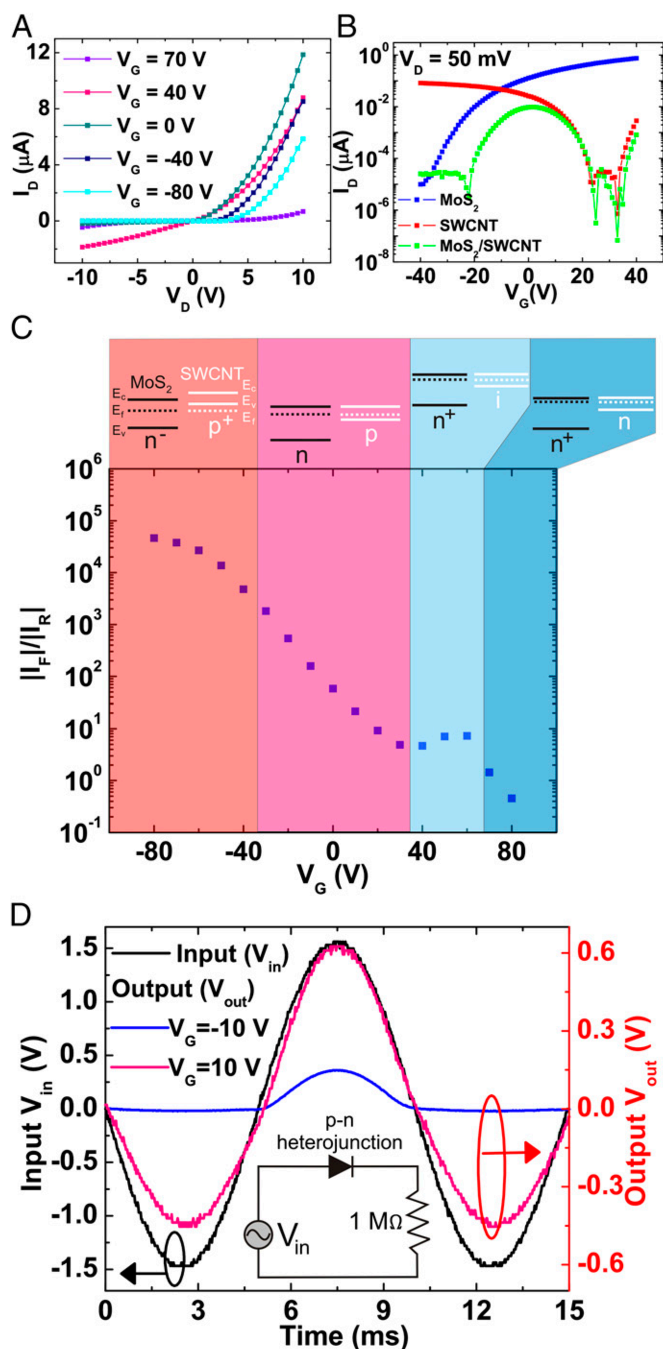

Fig. 2. Electrical properties of the s-SWCNT/SL-MoS_2 p-n heterojunction diode. (*A*) Gate-tunable output characteristics showing the transition from a nearly insulating state at V_G = 70 V to a conductive state with relatively poor rectification at V_G = 40 V to a highly rectifying diode behavior at negative gate voltages. (*B*) Transfer characteristics of the p-n junction (green), showing an antiambipolar characteristic, which is qualitatively a superposition of the transfer characteristics of the p-type s-SWCNT FET and n-type SL-MoS_2 FET. (*C*) Forward-to-reverse current ratio (at a heterojunction bias magnitude of 10 V) as a function of gate bias. The labels at the top show the corresponding band diagrams for the s-SWCNT/SL-MoS_2 p-n heterojunction. At a high positive gate bias, the formation of an n^+-n junction implies a low rectification ratio that transitions into an n^+-i junction (plateau region in the plot) with reducing V_G. The rectification ratio then rises with decreasing gate bias due to the formation of a p-n junction. (*D*) Demonstration of gate-tunable rectification using the p-n heterojunction diode. The *y* axis on the left shows the input voltage, whereas the *y* axis on the right shows the output voltage across the series resistor (1 MΩ). As a function of the gate bias, the device evolves from a nonrectifying resistor-like state at V_G = 10 V (magenta) to a diode-like rectifying state at V_G = -10 V (blue).

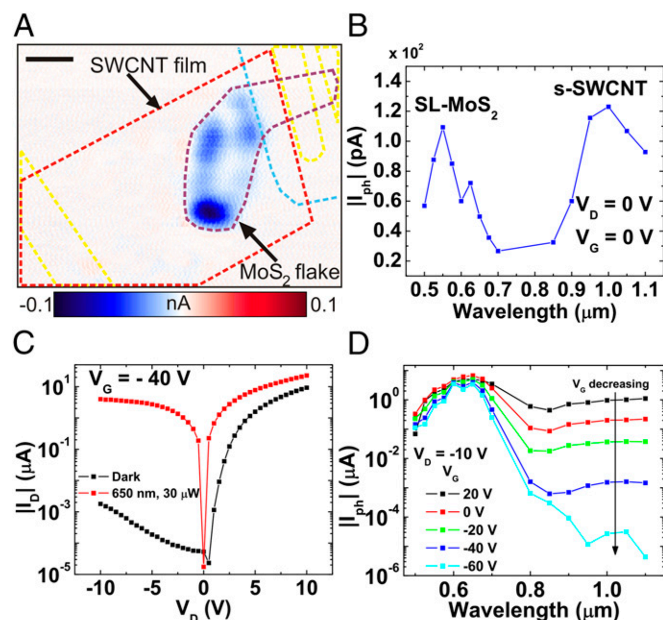

Fig. 3. Photoresponse of the p-n heterojunction. (*A*) Scanning photocurrent micrograph of a representative heterojunction device acquired at V_D (s-SWCNT electrode), V_G = 0 V showing the outlines of the SL-MoS_2 flake (purple dashed line) and the patterned s-SWCNT film (red dashed line) acquired at 700 nm with 20-μW power. Regions of large negative photocurrent (blue) are observed in the overlapping junction region. The patterned alumina and electrodes are indicated by cyan and yellow dashed lines, respectively. (*B*) Photocurrent spectrum of the junction under global illumination and zero bias conditions. The photocurrent magnitude is highest at the characteristic absorption energies of both SL-MoS_2 and s-SWCNTs. The photocurrent spectrum is acquired at the same incident power (30 μW). (*C*) Output curve of the same device in the dark and under global illumination at 650 nm. (*D*) Photocurrent spectral response can be tuned with the gate voltage. With decreasing gate voltage, the increased p-doping of the nanotubes and concomitant decreased n-doping of MoS_2 leads to a lower photocurrent in the near infrared region.

spectrum also likely has contributions from both SL-MoS_2 and the S_{33} transitions of s-SWCNTs because both absorb in that range of wavelengths (see *SI Text* for absorbance spectrum of SWCNTs).

To further illustrate the photoresponse of the s-SWCNT/SL-MoS_2 heterojunction, both output (*I-V*) and transfer curves (I-V_g) were acquired under global illumination at a series of wavelengths. A representative comparison of the dark and illuminated *I-V* curves at $V_G = -40$ V reveals that the photocurrent increases by four orders of magnitude at a heterojunction reverse bias of −5 V (Fig. 3*C*). Fig. 3*D* also shows the gate voltage-dependent photocurrent values at a heterojunction reverse bias of −10 V (Fig. 3*D*). As the gate voltage becomes more negative, the relative contribution from the s-SWCNT portion of the spectrum decreases, which is consistent with the s-SWCNT/SL-MoS_2 heterojunction becoming a p^+-n^- junction. Because the depletion region in a p-n junction extends farther into the side with lower doping/majority carrier concentration, the junction almost entirely lies in the SL-MoS_2 as it is depleted at negative V_G, leading to a reduced photocurrent contribution from the s-SWCNTs as observed in Fig. 3*D*. If we consider the junction from a molecular perspective used to describe organic semiconductor heterojunctions, one might also expect a change in the rate of charge transfer due to changes in band offsets [or Highest Occupied Molecular Orbitals (HOMO) and Lowest Unoccupied Molecular Orbitals (LUMO) levels] across the heterojunction.

With a strong photoresponse, the s-SWCNT/SL-MoS_2 heterojunction can be exploited as a photodetector. Diode-based

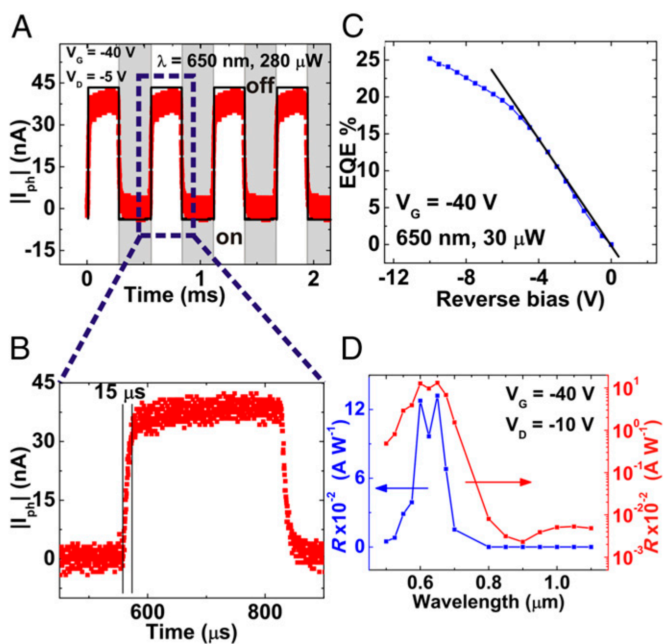

Fig. 4. Photodetection using the p-n heterojunction diode. (*A* and *B*) Time-dependent photoresponse of the p-n heterojunction showing fast rise and decay times of ~15 μs. (*C*) EQE as a function of reverse bias for the heterojunction at 650 nm. EQE increases linearly with reverse bias from 0 to −5 V with the highest EQE of 25% occurring at −10 V. (*D*) Spectrally dependent responsivity (*R*) of the photodiode in linear (blue) and logarithmic (red) scales. A large responsivity is observed for the absorption wavelengths of SL-MoS_2 compared with s-SWCNTs because the diode is being operated at $V_G = -40$ V (depletion mode of SL-MoS_2).

photodetectors are known for their fast photoresponse times compared with phototransistors because the photoexcited carriers must only traverse a distance equal to the depletion width of the junction. Indeed, we observe a fast photoresponse (<15 μs) from the s-SWCNT/SL-MoS_2 heterojunction as seen in Fig. 4 *A* and *B*. Importantly, this photoresponse time is orders of magnitude smaller than recently reported heterojunction phototransistors based on graphene (35). Furthermore, the s-SWCNT/SL-MoS_2 heterojunction photoresponse time reported here is limited by the rise time of the preamplifier used in these experiments, and thus 15 μs represents an upper bound.

The external quantum efficiency (EQE) of the s-SWCNT/SL-MoS_2 heterojunction photodetector is also noteworthy (~25% at $V_D = -10$ V) and compares favorably to other recently reported 2D nanomaterial heterostructures (Fig. 4*C*) (35–37). The EQE is calculated as $EQE = \frac{I_{ph}/e}{P/h\nu} \times 100$, where I_{ph}, e, P, and $h\nu$ represent the photocurrent, electronic charge, incident optical power, and photon energy, respectively. The linear rise in EQE at low reverse biases (Fig. 4*C*) is similar to the behavior of quantum dot (QD)-based photodiodes (38), which is related to changes in the depletion region. Here, given the negligible thickness of SL-MoS_2 compared with the expected depletion width (39), we attribute the increasing EQE to an increase in the rate of charge transfer across the heterojunction interface due to the change in band alignment rather than to an increase in the depletion width. The spectral responsivity (R) of the heterojunction photodetector is presented in Fig. 4*D*. The highest R exceeds 0.1 A/W at a wavelength of 650 nm, which is comparable to other nanostructured diode-based photodetectors in the literature (40). The combination of high R and fast photoresponse time presents distinct advantages over currently available organic and QD photodiodes (38).

In conclusion, we demonstrated a gate-tunable p-n heterojunction diode through the integration of p-type s-SWCNTs and n-type SL-MoS_2. The ultrathin nature of the constituent materials implies that both components can be modulated by a capacitively coupled gate bias, thereby enabling wide tunability of charge transport from a nearly insulating state to a highly rectifying condition with forward-to-reverse bias current ratios exceeding 10^4. When operated as a three-terminal device, the p-n heterojunction diode also shows antiambipolar behavior with current on/off ratios greater than 10^4, suggesting its utility in advanced logic applications. Furthermore, because s-SWCNTs and SL-MoS_2 are direct band gap semiconductors, the p-n heterojunction diode serves as an effective photodetector with fast photoresponse <15 μs. By combining other chirality resolved s-SWCNTs (41) with the growing list of 2D semiconductor nanomaterials (42–45), the p-n heterojunction diode can be generalized to a wide range of electronic and optoelectronic applications.

ACKNOWLEDGMENTS. We acknowledge discussions with J. M. P. Alaboson and thank B. Myers and I. S. Kim for assistance with electron beam lithography and Raman spectroscopy, respectively. This work was supported by the Materials Research Science and Engineering Center (MRSEC) of Northwestern University [National Science Foundation (NSF) Grant DMR-1121262] and the Office of Naval Research Multidisciplinary University Research Initiative Program (N00014-11-1-0690). M.L.G. also acknowledges an NSF Graduate Research Fellowship. This research made use of the Northwestern University's Atomic and Nanoscale Characterization Experimental Center at Northwestern University, which is supported by the NSF-Nanoscale Science and Engineering Center, NSF-MRSEC, Keck Foundation, and State of Illinois. This research also used the Northwestern University Micro/Nano Fabrication cleanroom facility at Northwestern University.

1. Schwierz F (2010) Graphene transistors. *Nat Nanotechnol* 5(7):487–496.
2. Jariwala D, Sangwan VK, Lauhon LJ, Marks TJ, Hersam MC (2013) Carbon nanomaterials for electronics, optoelectronics, photovoltaics, and sensing. *Chem Soc Rev* 42(7):2824–2860.
3. Banerjee SK, et al. (2010) Graphene for CMOS and beyond CMOS applications. *Proc IEEE* 98(12):2032–2046.
4. Britnell L, et al. (2012) Field-effect tunneling transistor based on vertical graphene heterostructures. *Science* 335(6071):947–950.
5. Georgiou T, et al. (2013) Vertical field-effect transistor based on graphene-WS_2 heterostructures for flexible and transparent electronics. *Nat Nanotechnol* 8(2):100–103.
6. Dean CR, et al. (2010) Boron nitride substrates for high-quality graphene electronics. *Nat Nanotechnol* 5(10):722–726.
7. Yang H, et al. (2012) Graphene barristor, a triode device with a gate-controlled Schottky barrier. *Science* 336(6085):1140–1143.
8. Yu WJ, et al. (2013) Vertically stacked multi-heterostructures of layered materials for logic transistors and complementary inverters. *Nat Mater* 12(3):246–252.
9. Choi MS, et al. (2013) Controlled charge trapping by molybdenum disulphide and graphene in ultrathin heterostructured memory devices. *Nat Commun* 4:1624.
10. Bertolazzi S, Krasnozhon D, Kis A (2013) Nonvolatile memory cells based on MoS_2/graphene heterostructures. *ACS Nano* 7(4):3246–3252.
11. Britnell L, et al. (2013) Resonant tunnelling and negative differential conductance in graphene transistors. *Nat Commun* 4:1794.
12. Ponomarenko L, et al. (2011) Tunable metal-insulator transition in double-layer graphene heterostructures. *Nat Phys* 7(12):958–961.
13. Kim S, et al. (2011) Coulomb drag of massless fermions in graphene. *Phys Rev B* 83(16):161401.
14. Kim S, et al. (2012) Direct measurement of the Fermi energy in graphene using a double-layer heterostructure. *Phys Rev Lett* 108(11):116404.
15. Levendorf MP, et al. (2012) Graphene and boron nitride lateral heterostructures for atomically thin circuitry. *Nature* 488(7413):627–632.
16. Ci L, et al. (2010) Atomic layers of hybridized boron nitride and graphene domains. *Nat Mater* 9(5):430–435.
17. Liu Z, et al. (2013) In-plane heterostructures of graphene and hexagonal boron nitride with controlled domain sizes. *Nat Nanotechnol* 8(2):119–124.
18. Wei P, et al. (2013) Tuning the Dirac point in CVD-grown graphene through solution processed n-type doping with 2-(2-methoxyphenyl)-1,3-dimethyl-2,3-dihydro-1H-benzoimidazole. *Nano Lett* 13(5):1890–1897.
19. Williams JR, Dicarlo L, Marcus CM (2007) Quantum Hall effect in a gate-controlled p-n junction of graphene. *Science* 317(5838):638–641.
20. Collins PG, Bradley K, Ishigami M, Zettl A (2000) Extreme oxygen sensitivity of electronic properties of carbon nanotubes. *Science* 287(5459):1801–1804.
21. Radisavljevic B, Radenovic A, Brivio J, Giacometti V, Kis A (2011) Single-layer MoS_2 transistors. *Nat Nanotechnol* 6(3):147–150.

22. Jariwala D, et al. (2013) Band-like transport in high mobility unencapsulated single-layer MoS_2 transistors. *Appl Phys Lett* 102(17):173107.
23. Sangwan VK, et al. (2012) Fundamental performance limits of carbon nanotube thin-film transistors achieved using hybrid molecular dielectrics. *ACS Nano* 6(8):7480–7488.
24. Arnold MS, Green AA, Hulvat JF, Stupp SI, Hersam MC (2006) Sorting carbon nanotubes by electronic structure using density differentiation. *Nat Nanotechnol* 1(1):60–65.
25. Behnam A, et al. (2013) High-field transport and thermal reliability of sorted carbon nanotube network devices. *ACS Nano* 7(1):482–490.
26. Liu H, Neal AT, Ye PD (2012) Channel length scaling of MoS_2 MOSFETs. *ACS Nano* 6(10):8563–8569.
27. Mak KF, et al. (2013) Tightly bound trions in monolayer MoS_2. *Nat Mater* 12(3): 207–211.
28. Mueller T, et al. (2010) Efficient narrow-band light emission from a single carbon nanotube p-n diode. *Nat Nanotechnol* 5(1):27–31.
29. Liu C-H, Wu C-C, Zhong Z (2011) A fully tunable single-walled carbon nanotube diode. *Nano Lett* 11(4):1782–1785.
30. Chuang S, et al. (2013) Near-ideal electrical properties of InAs/WSe_2 van der Waals heterojunction diodes. *Appl Phys Lett* 102(24):242101.
31. Mak KF, Lee C, Hone J, Shan J, Heinz TF (2010) Atomically thin MoS_2: A new direct-gap semiconductor. *Phys Rev Lett* 105(13):136805.
32. O'Connell MJ, et al. (2002) Band gap fluorescence from individual single-walled carbon nanotubes. *Science* 297(5581):593–596.
33. Sczygelski E, et al. (2013) Extrinsic and intrinsic photoresponse in monodisperse carbon nanotube thin film transistors. *Appl Phys Lett* 102(8):083104.
34. Wu C-C, et al. (2013) Elucidating the photoresponse of ultrathin MoS_2 field-effect transistors by scanning photocurrent microscopy. *J. Phys. Chem. Lett.* 4(15):2508–2513.
35. Konstantatos G, et al. (2012) Hybrid graphene-quantum dot phototransistors with ultrahigh gain. *Nat Nanotechnol* 7(6):363–368.
36. Britnell L, et al. (2013) Strong light-matter interactions in heterostructures of atomically thin films. *Science* 340(6138):1311–1314.
37. Zhang W, et al. (2013) Ultrahigh-gain phototransistors based on graphene-MoS_2 heterostructures. arXiv preprint arXiv:1302.1230.
38. Rauch T, et al. (2009) Near-infrared imaging with quantum-dot-sensitized organic photodiodes. *Nat Photonics* 3(6):332–336.
39. Li Y, Xu C-Y, Zhen L (2013) Surface potential and interlayer screening effects of few-layer MoS_2 nanoflakes. *Appl Phys Lett* 102(14):143110.
40. Konstantatos G, Sargent EH (2010) Nanostructured materials for photon detection. *Nat Nanotechnol* 5(6):391–400.
41. Green AA, Hersam MC (2011) Nearly single-chirality single-walled carbon nanotubes produced via orthogonal iterative density gradient ultracentrifugation. *Adv Mater* 23(19):2185–2190.
42. Wang QH, Kalantar-Zadeh K, Kis A, Coleman JN, Strano MS (2012) Electronics and optoelectronics of two-dimensional transition metal dichalcogenides. *Nat Nanotechnol* 7(11):699–712.
43. Fang H, et al. (2013) Degenerate n-doping of few-layer transition metal dichalcogenides by potassium. *Nano Lett* 13(5):1991–1995.
44. Fang H, et al. (2012) High-performance single layered WSe_2 p-FETs with chemically doped contacts. *Nano Lett* 12(7):3788–3792.
45. Braga D, Gutiérrez Lezama I, Berger H, Morpurgo AF (2012) Quantitative determination of the band gap of WS_2 with ambipolar ionic liquid-gated transistors. *Nano Lett* 12(10):5218–5223.

Supporting Information

Jariwala et al. 10.1073/pnas.1317226110

SI Text

Materials and Device Fabrication. ***Raman spectroscopy of MoS_2.*** The monolayer character of the MoS_2 flake samples was confirmed via Raman spectroscopy. The Raman spectra were acquired using a 532-nm laser with a 100× objective (NA = 0.9) in a scanning confocal microscope (WITec Alpha300 R). The separation between E_{2g} and A_{1g} modes of MoS_2 (Δ) is a well-known parameter for identifying layer thickness in ultrathin MoS_2 flakes. Typically, a Δ value of <20 cm^{-1} indicates a single layer sample (1). Fig. S1 shows the Raman spectrum ($\Delta\sim$ 17.7 cm^{-1}) of a representative flake that was fabricated into a p-n heterojunction device.

Sorting and deposition of semiconducting single-walled carbon nanotubes. Semiconducting single-walled carbon nanotubes (SWCNTs) with ∼99% semiconductor purity were isolated by density gradient ultracentrifugation following the procedure discussed in a previous report (2). SWCNT thin films were prepared by vacuum filtration and transferred onto prepatterned Au electrodes by the acetone bath transfer method as outlined in the literature (2, 3). The semiconducting purity of the sorted SWCNTs was estimated using the optical absorbance characterization and an analysis protocol developed earlier (3, 4). Fig. S2 shows the optical absorbance spectra for as-purchased arc-discharge SWCNTs (P2; Carbon Solutions) and sorted ∼99% semiconductor purity SWCNTs. The average diameter of the semiconducting tubes is 1.4 nm.

All devices were fabricated on 300-nm-thick SiO_2/Si substrates. The Si <100> wafers were purchased from Silicon Quest International. The wafers were doped n-type with As (resistivity = 0.001–0.005 Ω-cm). The MoS_2 field-effect transistors (FETs) were fabricated using previously reported techniques (5). Specifically, bulk MoS_2 crystals were purchased from SPI Supplies and mechanically exfoliated using clear adhesive tape. The flakes were identified using an optical microscope (Olympus BX 51M) and then subjected to electron beam lithography (EBL). A two-step EBL process was adopted to fabricate Au contacts with no adhesion layer. The patterns in the first step were designed to be just short of touching the MoS_2 flakes. Au (75 nm thick) is the metal in contact with the MoS_2 flake. Following liftoff in acetone, the devices were further cleaned with remover PG (Microchem) at 60 °C for 1 h.

A portion of the MoS_2 FET including both the contacts and channel was exposed in a subsequent step of EBL. Atomic layer deposition (ALD; Cambridge Nanotech, Savannah S100) was used to grow 30-nm alumina at 100 °C to insulate the MoS_2 channel and contacts, thus prevent shorting following subsequent SWCNT deposition. Trimethyl aluminum (TMA) (Aldrich, 99%) was used as the precursor for ALD growth of alumina, and ultrahigh purity nitrogen (Airgas) was used as the purging gas. A single ALD cycle consisted of a TMA pulse for 0.015 s and a 30-s purge, followed by a H_2O pulse for 0.015 s and a second 30-s purge. The growth rate was determined to be ∼0.75 Å/cycle. A total of 400 cycles was performed to achieve 30 nm thickness. The oxide was lifted off in warm acetone at 50 °C for 1 h. A cellulose membrane containing the semiconducting SWCNT film was then stamped onto the entire substrate and dissolved under acetone vapor as outlined in previous reports (2). The SWCNT film was annealed in vacuum (50 mTorr) at 200 °C for 1 h and then patterned with EBL using a ZEP 150 (Nippon Zeon) resist. Reactive ion etching (Samco RIE-10 NR) in an oxygen plasma atmosphere (100 mW, 15 s, 20 sccm) was then used to etch the nanotubes. The resist was subsequently dissolved in hot (80 °C) *N*-methyl-2- pyrrolidone for ∼6 h. The SWCNT film morphology close to the junction region was characterized using AFM as shown in Fig. S3.

Electrical and Photocurrent Measurements. Output and transfer characteristics were measured using Keithley 2400 source meters and custom LabView programs. The gate voltage was swept at 10 V/s in steps of 1 V in the transfer and output plots shown in Fig. 2*B*.

The p-n heterojunction diode was used as a half-wave rectifier using the circuit outlined in the inset of Fig. 2*D*. A 1-MΩ resistor was used in series with the device to limit the current. A sinusoidal wave from a waveform generator was used as the input, whereas the output current was measured using a preamplifier (1211 DL Instruments) and the output voltage as it would appear across a 1-MΩ resistor (schematic in Fig. 2*D*). Time domain waveforms were captured using an oscilloscope.

A scanning confocal microscope (100× objective with NA = 0.9; WiTec system) coupled to a tunable coherent white light source (NKT Photonics) was used to generate the spatially resolved photocurrent, which was converted into a voltage by a current preamplifier and recorded by either a lock-in amplifier (for imaging) or a digital sampling oscilloscope (for temporally resolved measurements). The junction area was subjected to global illumination using the same apparatus with a 20× objective. The current-voltage (*I-V*) characteristics under global illumination were acquired using the same Keithley 2400 source meters and custom LabView programs.

Analysis of Current Voltage Characteristics. ***Junction transfer characteristics, contact resistance, and sheet resistance.*** Linear and semi-log transfer characteristics of the junction are shown in Fig. S4. The channel resistances of the individual MoS_2 and CNT FETs were estimated at $V_G = 0$ V by subtracting the contact resistance values reported in literature from the $(dI/dV)^{-1}$ values obtained using the *I-V* plots shown in Fig. S5. The channel resistance of the CNT FET at $V_G = 0$ V is estimated to be ∼0.66 MΩ, whereas that of the MoS_2 FET is ∼0.39 MΩ. These channel resistance values are >15 times smaller than the junction resistance $[(dI/dV)^{-1}$ near $V_D = 0$ V] of ∼11.6 MΩ obtained from Fig. 2*A*. Assuming that the length of the nonjunction portions of single layer (SL)-MoS_2 and s-SWCNT film are the same as their respective FET channels, the resistance of the junction after subtracting the series resistances of the nonjunction portions and the contact resistances is about 10.4 MΩ. Thus, the junction resistance dominates even in presence of series resistances at $V_G = 0$. However, this situation changes under depletion gate biases of either the s-SWCNTs or MoS_2, which leads to the antiambipolar behavior with two off states at either extremes in gate voltage.

Data fitting to the Shockley equation. The diode output curves with varying gate bias (V_G) were fit with the Shockley diode equation, $|I_D| = |I_{rs}|\left(e^{\frac{eV_D}{nk_BT}} - 1\right)$, where I_D is the drain current, V_D is the drain bias, I_{rs} is the reverse saturation current at $V_D = -0.05$ V, e is the electronic charge, n is the ideality factor, k_B is the Boltzmann constant, and T is the temperature of operation (300 K). The best fit to the diode curve ($r^2 > 99\%$) is achieved for V_G values ranging from −30 to −60 V, with the diode ideality factor (n) approaching closest to 1 at −40 V (Fig. S6). The *I-V* curves at other gate biases fit poorly to the Shockley equation ($r^2 < 70\%$).

Spatial Mapping of Photoluminescence and Raman Shift. Spatial Raman and photoluminescence (PL) mapping was performed on

the heterojunction device. A spatial map of the Raman 2G peak (3,100–3,250 cm^{-1}) from the SWCNTs and photoluminescence from the SL-MoS_2 at 3,700–3,900 cm^{-1} (A peak) shows that the photocurrent arises only from the junction region. It was also observed that that the PL signal was uniform in the junction area of the MoS_2 flake compared with the protected/masked area as seen in Fig. S7.

Power dependence of photocurrent. The power dependence of the photocurrent was measured under zero bias using the same illumination system (Fig. S8). The power dependence is sublinear, which is consistent with bimolecular recombination of electrons and holes, further implying that the concentration of photogenerated carriers is similar to or greater than the intrinsic carrier concentration (6).

Calculation of responsivity and quantum efficiency. The quantum efficiency was calculated using the formula $EQE = \frac{I_{ph}/e}{P/h\nu} \times 100$, where I_{ph}, e, P, and $h\nu$ represent the photocurrent, electronic charge, incident optical power, and photon energy, respectively. The photocurrent was extracted by subtracting the dark *I-V* curves from the illuminated *I-V* curves. The responsivity (R) was calculated using $R = EQE \times 1.24/\lambda$, where λ is in micrometers.

1. Lee C, et al. (2010) Anomalous lattice vibrations of single- and few-layer MoS_2. *ACS Nano* 4(5):2695–2700.
2. Sangwan VK, et al. (2012) Fundamental performance limits of carbon nanotube thin-film transistors achieved using hybrid molecular dielectrics. *ACS Nano* 6(8):7480–7488.
3. Green AA, Hersam MC (2011) Nearly single-chirality single-walled carbon nanotubes produced via orthogonal iterative density gradient ultracentrifugation. *Adv Mater* 23(19):2185–2190.
4. Arnold MS, Green AA, Hulvat JF, Stupp SI, Hersam MC (2006) Sorting carbon nanotubes by electronic structure using density differentiation. *Nat Nanotechnol* 1(1):60–65.
5. Jariwala D, et al. (2013) Band-like transport in high mobility unencapsulated single-layer MoS_2 transistors. *Appl Phys Lett* 102(17):173107.
6. Bube RH (1992) *Photoelectronic Properties of Semiconductors* (Cambridge Univ Press, Cambridge, UK).

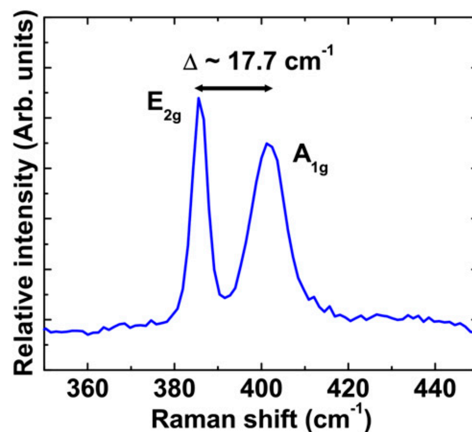

Fig. S1. Raman spectrum of a representative MoS_2 flake. The separation of 17.7 cm^{-1} between the E_{2g} and A_{1g} features indicates monolayer thickness.

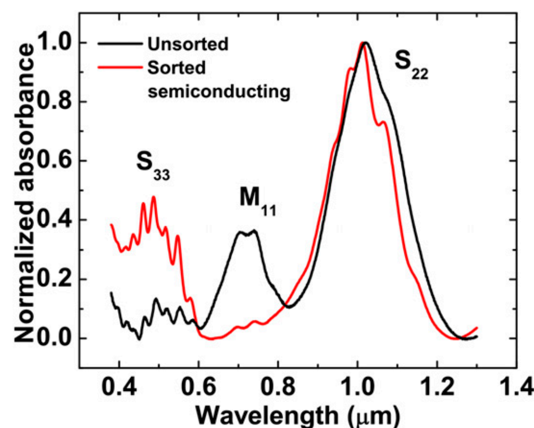

Fig. S2. Normalized optical absorbance spectra of arc discharge SWCNTs. The unsorted SWCNTs (black) consist of a mixture of metallic and semiconducting species as evidenced by the presence of both semiconducting (S_{22} and S_{33}) and metallic (M_{11}) peaks, whereas the spectrum of the sorted semiconducting SWCNTs (red) shows strong semiconducting peaks and negligible metallic peaks.

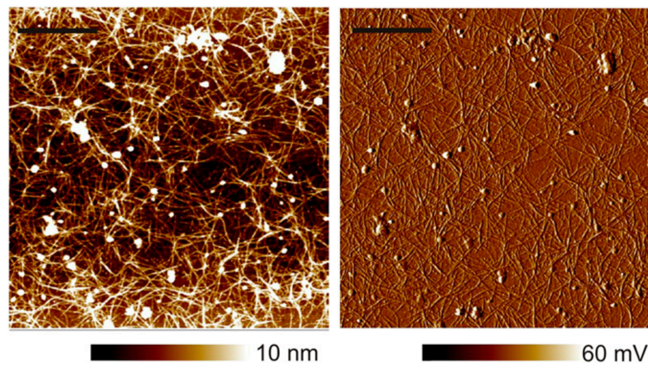

Fig. S3. Atomic force microscopy (AFM) images of the SWCNT film. Topographic image (*Left*) and amplitude error (*Right*) show the random network morphology and uniform coverage of SWCNTs. (Scale bar, 1.5 μm.)

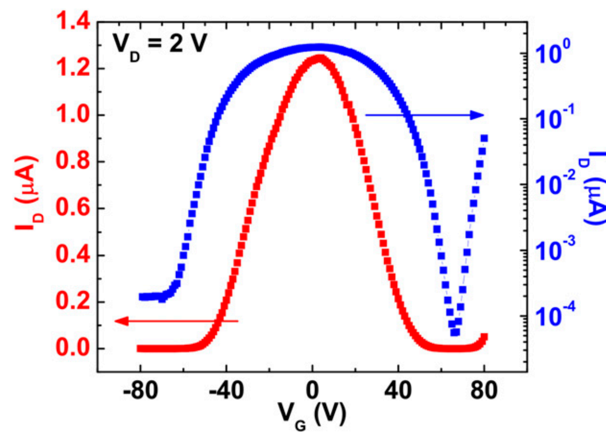

Fig. S4. Linear (red) and semilog (blue) transfer characteristics of a representative p-n heterojunction diode showing antiambipolar behavior and on/off ratio exceeding 10^4.

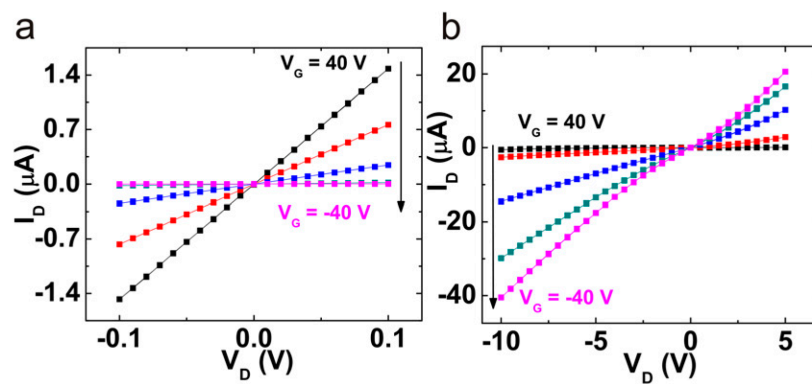

Fig. S5. (*A*) Output plots of a representative SL-MoS_2 FET showing linear *I-V* characteristics and n-type behavior. (*B*) Output plots of a representative s-SWCNT FET showing p-type behavior.

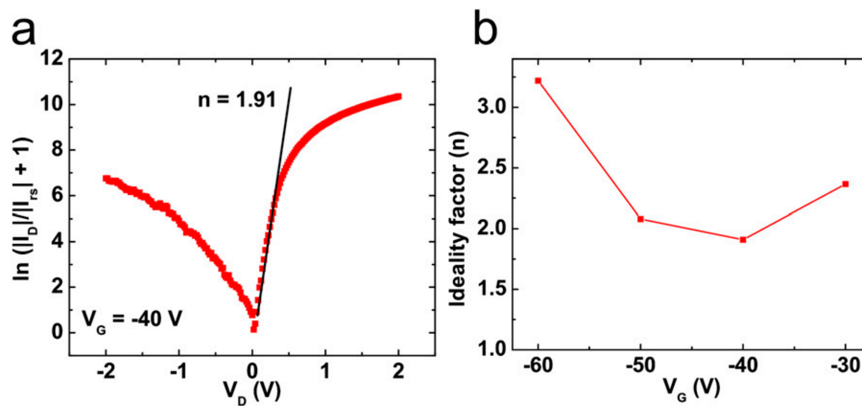

Fig. S6. (*A*) Shockley diode equation fit to the output curve at $V_G = -40$ V. (*B*) Variation of n with V_G shows that the diode is closest to ideal behavior at $V_G = -40$ V.

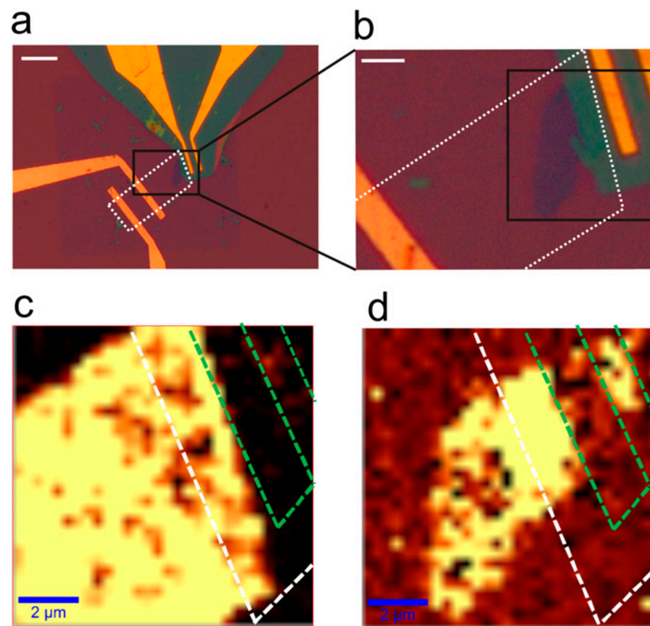

Fig. S7. (*A*) Optical micrograph of a heterojunction device showing a SL-MoS_2 FET top right and s-SWCNT FET bottom left. The white dotted line indicates the extent of the patterned SWCNT film. (Scale bar, 10 μm.) (*B*) Zoom-in of *A* representing the area scanned for spatial photocurrent mapping in Fig. 3*A*. The black outline indicates the scanned area for spatial mapping of the PL and the Raman shift. (Scale bar, 2.5 μm.) (*C*) Spatial map of the Raman shift (3,100–3,250 cm^{-1}), which shows the bright area as the patterned SWCNT film. No Raman signal for the SWCNTs is observed in the MoS_2 contact or channel region marked by green lines. The white boundary indicates the extent of ALD grown alumina. (*D*) PL map of the SL-MoS_2 flake at the A peak (3,700–3,900 cm^{-1}). The region of increased PL intensity represents the shape of the flake as seen in the optical images and the photocurrent map of Fig. 3*A*. No PL signal is observed in the contact regions, indicating PL quenching by the gold. PL from MoS_2 is also observed from the SL-MoS_2 FET channel area, between the contacts.

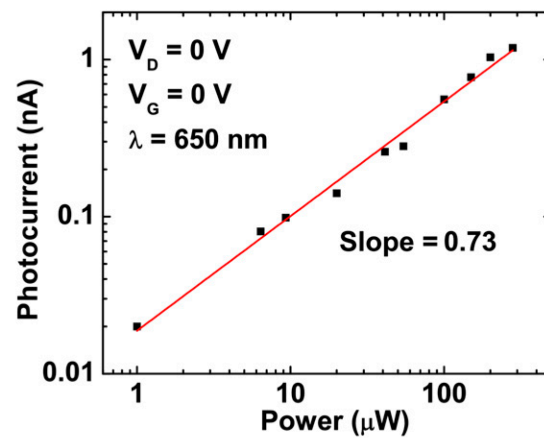

Fig. S8. Power dependence of the photocurrent under zero applied bias. The red line is a linear fit to the data showing a slope of 0.73.